

## RESEARCH ARTICLE

View Article Online

View Journal | View Issue



Cite this: *Inorg. Chem. Front.*, 2022, **9**, 5926

# Highly efficient electrochemical CO<sub>2</sub> reduction over crystalline–amorphous In<sub>2</sub>O<sub>3</sub>–CeO<sub>x</sub> heterostructures†

Cuifeng Wang, Zhaohui Wu, Guihao Liu, Sha Bai, Lin Guo, Lei He \* and Yu-Fei Song \*

The electrochemical reduction reaction of CO<sub>2</sub> (CO<sub>2</sub>RR) to fuels and chemicals is a promising approach to consume greenhouse gases and mitigate the dependence on fossil fuels. Herein, we synthesized an effective crystalline–amorphous In<sub>2</sub>O<sub>3</sub>–CeO<sub>x</sub> heterostructure, which exhibited high catalytic performance for CO<sub>2</sub>-to-formate conversion. The maximum faradaic efficiency (FE) of 94.8% was achieved, and above 90% FE can be maintained in a wide potential range from –0.8 to –1.2 V vs. RHE. Detailed studies showed that In<sub>2</sub>O<sub>3</sub> functioned as the active site for CO<sub>2</sub> activation and formate formation, and the amorphous CeO<sub>x</sub> was beneficial for the electron transfer, leading to the electronic structure reconfiguration of In<sub>2</sub>O<sub>3</sub>. Hence, the In<sub>2</sub>O<sub>3</sub>–CeO<sub>x</sub> heterostructure enhanced the adsorption of \*OCHO intermediates and lowered the energy barrier forming \*HCOOH from \*OCHO.

Received 29th July 2022,  
Accepted 29th September 2022

DOI: 10.1039/d2qi01646j

rsc.li/frontiers-inorganic

## Introduction

The electrochemical reduction reaction of CO<sub>2</sub> (CO<sub>2</sub>RR) into value-added chemicals and fuels is a promising approach to consume excess industrial CO<sub>2</sub> emissions and address the current ongoing consumption of non-renewable fossil fuels.<sup>1–4</sup> Nevertheless, there are still problems restricting the practical application of the CO<sub>2</sub>RR. For example, CO<sub>2</sub> gas molecules are thermodynamically stable, and the complexity of the reaction pathway as well as the competitive hydrogen evolution reaction (HER) leads to diverse products and low selectivity. Considering the cost of electricity and the product's market price, the two-electron transfer products formate and CO are the most promising target products among the numerous CO<sub>2</sub> reduction products.<sup>5</sup> Formate is one of the fundamental starting materials for industrial production, which is widely used in the fields of pesticides, dyes, medicine, rubber and tanning industries.<sup>6</sup> As such, efficient catalysts need to be developed to lower the energy barrier and improve the selectivity for converting CO<sub>2</sub> to formate.

The p-block metals such as In, Bi, Pb, and Sn are efficient catalysts for CO<sub>2</sub> electroreduction due to their high overpotential for the HER.<sup>7–10</sup> Among them, low-toxicity and environmentally friendly In-based materials show high selectivity to formate.<sup>11</sup>

Various strategies on In-based catalysts have been proposed such as morphology design,<sup>12</sup> defect engineering,<sup>13</sup> doping,<sup>14</sup> and alloying<sup>15</sup> to reinforce the catalytic activities. Although these strategies are ingenious in design, they still suffer from cumbersome synthetic procedures, and the electrochemical performance still needs to be further improved. As such, the development of novel In-based catalysts is promising for electroreduction of CO<sub>2</sub> to formate.

Constructing heterostructures is an effective strategy to enhance the electrocatalytic performance due to their efficient charge transfer at the interface and the sufficiently exposed catalytically active sites.<sup>16–18</sup> In particular, heterostructures can direct high selectivity toward a specific product in complicated CO<sub>2</sub>RR reaction routes *via* adjusting the binding strength with key intermediates.<sup>19,20</sup> CeO<sub>2</sub>-based materials possess unique transformation characteristics between Ce<sup>3+</sup> and Ce<sup>4+</sup> states, which are beneficial for the gain and loss of electrons,<sup>21</sup> and have been proved to significantly strengthen the adsorption and promote the activation of CO<sub>2</sub> molecules. These properties make CeO<sub>2</sub> suitable for constructing heterostructures to enhance the CO<sub>2</sub> conversion process. For example, Bao *et al.*<sup>22</sup> have demonstrated that the CO<sub>2</sub>RR can be significantly improved by the interface of Au–CeO<sub>x</sub> heterostructures. Gong *et al.*<sup>23</sup> have revealed that high Ce<sup>3+</sup> concentration is beneficial for CO<sub>2</sub> activation. Notably, in comparison with their crystalline–crystalline counterparts, crystalline–amorphous heterostructures can inherit the merits of amorphous structures, such as abundant active sites and defects, high flexibility, and better corrosion resistance.<sup>24,25</sup> Therefore, rational design of crystalline–amorphous heterostructures is an effective method to achieve the purpose of improving CO<sub>2</sub>RR performance.

State Key Laboratory of Chemical Resource Engineering, Beijing University of Chemical Technology, Beijing 100029, P. R. China. E-mail: helei@mail.buct.edu.cn, songyuf@mail.buct.edu.cn; Fax: +86 10 64431832; Tel: +86 10 64431832

† Electronic supplementary information (ESI) available. See DOI: <https://doi.org/10.1039/d2qi01646j>

Herein, crystalline–amorphous  $\text{In}_2\text{O}_3\text{--CeO}_x$  heterostructures were fabricated for the first time and were used as an electro-catalyst for the  $\text{CO}_2\text{RR}$ . It was discovered that the maximum faradaic efficiency (FE) can reach 94.8% at  $-0.9\text{ V}$  vs. RHE over  $\text{In}_2\text{O}_3\text{--CeO}_x$ , which was obviously more efficient than those of a pure  $\text{In}_2\text{O}_3$  catalyst and a crystalline–crystalline  $\text{In}_2\text{O}_3\text{--CeO}_2$  heterostructure. The improved performance of the  $\text{In}_2\text{O}_3\text{--CeO}_x$  catalyst was attributed to the electronic reconfiguration of indium by strengthened electron transfer between  $\text{In}_2\text{O}_3$  and amorphous  $\text{CeO}_x$ , which significantly enhanced the adsorption of  $^*\text{OCHO}$  intermediates and lowered the energy barrier of  $^*\text{OCHO} \rightarrow ^*\text{HCOOH}$ , leading to the high activity and selectivity for the  $\text{CO}_2\text{RR}$  to formate.

## Results and discussion

The  $\text{In}_2\text{O}_3\text{--CeO}_x$  catalyst was synthesized *via* two steps (Fig. S1a†). Firstly, an aqueous solution containing indium nitrate, sodium carbonate and as-prepared  $\text{CeO}_x$  was stirred to form an  $\text{In}(\text{OH})_3\text{--CeO}_x$  precipitate for one hour at room temperature. Secondly, the precursor  $\text{In}(\text{OH})_3\text{--CeO}_x$  was annealed under an  $\text{Ar}/\text{H}_2$  flow for one hour to obtain the  $\text{In}_2\text{O}_3\text{--CeO}_x$  catalyst. The structures of the samples (*e.g.*,  $\text{In}_2\text{O}_3\text{--CeO}_x$ ,  $\text{In}_2\text{O}_3\text{--CeO}_2$ , the individual  $\text{CeO}_x$ ,  $\text{CeO}_2$  and  $\text{In}_2\text{O}_3$ ) were determined using X-ray diffraction (XRD) patterns. As shown in Fig. 1a, no obvious peak was observed for  $\text{CeO}_x$ , suggesting that the amorphous structure was successfully achieved. In addition, no obvious peak of  $\text{In}_2\text{O}_3$  was observed in the  $\text{In}_2\text{O}_3\text{--CeO}_x$  sample, which was caused by the small particle size and uniform dispersion of  $\text{In}_2\text{O}_3$ . In contrast,  $\text{CeO}_2$  displayed the characteristic peaks of the crystal structure, which were consistent with those reported in the literature (Fig. 1b).<sup>26</sup> The

peaks of  $\text{In}_2\text{O}_3\text{--CeO}_2$  matched well with the standard patterns of  $\text{CeO}_2$  and  $\text{In}_2\text{O}_3$ , as shown in Fig. 1b. The high-resolution transmission electron microscopy (HR-TEM) images showed the crystalline–amorphous heterostructure interface of  $\text{In}_2\text{O}_3\text{--CeO}_x$  and crystalline–crystalline heterostructure interface of  $\text{In}_2\text{O}_3\text{--CeO}_2$  (Fig. 1c–f). As shown in Fig. 1d, the lattice fringe of  $\text{In}_2\text{O}_3\text{--CeO}_x$  could be assigned to the (222) plane of  $\text{In}_2\text{O}_3$  while the amorphous  $\text{CeO}_x$  did not show any lattice stripes. In contrast, the HR-TEM image of  $\text{In}_2\text{O}_3\text{--CeO}_2$  clearly presented the lattice fringes for the (222) facet of  $\text{In}_2\text{O}_3$  and (111) facet of  $\text{CeO}_2$  (Fig. 1f). Furthermore, energy dispersive X-ray spectroscopy (EDX) elemental mapping of the samples showed that In, Ce, and O were evenly distributed (Fig. 1g–j and S2†), confirming the successful preparation of  $\text{In}_2\text{O}_3\text{--CeO}_x$  and  $\text{In}_2\text{O}_3\text{--CeO}_2$  heterostructures.

X-ray photoelectron spectroscopy (XPS) was utilized to investigate the electronic properties and chemical compositions of the samples. The Ce 3d XPS spectra of  $\text{CeO}_x$  showed the presence of both  $\text{Ce}^{4+}$  and  $\text{Ce}^{3+}$  peaks (Fig. 2a), where  $\text{Ce}^{3+}$  included one pair of peaks (V and V'), whilst  $\text{Ce}^{4+}$  had two pairs of peaks ( $U_1$ ,  $U_2$ ,  $U'_1$ , and  $U'_2$ ). Notably, the proportion of  $\text{Ce}^{3+}$  in  $\text{In}_2\text{O}_3\text{--CeO}_x$  was increased to 48.3% (Fig. 2b) compared to the individual  $\text{CeO}_x$  (43.2%). In contrast, the proportion of  $\text{Ce}^{3+}$  in  $\text{In}_2\text{O}_3\text{--CeO}_2$  showed no obvious variation compared to that in  $\text{CeO}_2$  (Fig. S3a and b†). Additionally, the In 3d spectra of  $\text{In}_2\text{O}_3$  showed two peaks at 451.7 (In  $3d_{3/2}$ ) and 444.2 eV (In  $3d_{5/2}$ ), while the binding energy of In 3d in  $\text{In}_2\text{O}_3\text{--CeO}_x$  shifted positively about 1 eV compared to that of  $\text{In}_2\text{O}_3$  (Fig. 2c). The results demonstrated the strong interaction between  $\text{In}_2\text{O}_3$  and  $\text{CeO}_x$ , and electrons transferred from the crystalline  $\text{In}_2\text{O}_3$  to amorphous  $\text{CeO}_x$ , which led to an increase in the proportion of  $\text{Ce}^{3+}$  in  $\text{In}_2\text{O}_3\text{--CeO}_x$ . Moreover, the linear sweep voltammetry (LSV) curves of  $\text{In}_2\text{O}_3$  showed an obvious reduction peak at

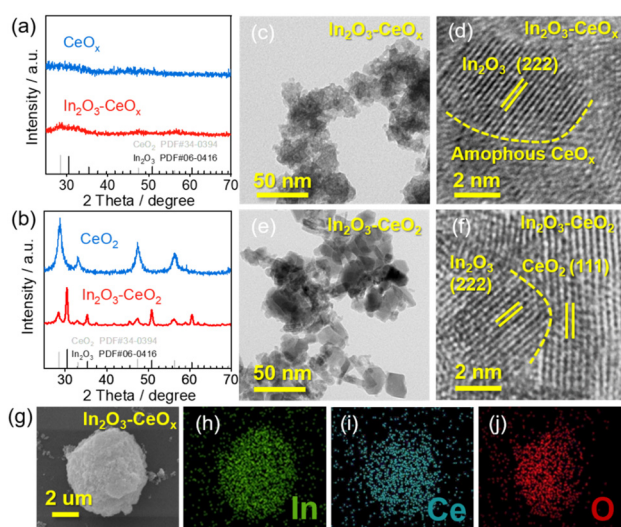


**Fig. 1** (a) XRD patterns of  $\text{CeO}_x$  and  $\text{In}_2\text{O}_3\text{--CeO}_x$ , (b) XRD patterns of  $\text{CeO}_2$  and  $\text{In}_2\text{O}_3\text{--CeO}_2$ , (c) and (d) HR-TEM image of  $\text{In}_2\text{O}_3\text{--CeO}_x$  and (e) and (f) HR-TEM image of  $\text{In}_2\text{O}_3\text{--CeO}_2$ . (g–j) The corresponding EDX elemental mapping of  $\text{In}_2\text{O}_3\text{--CeO}_x$ .

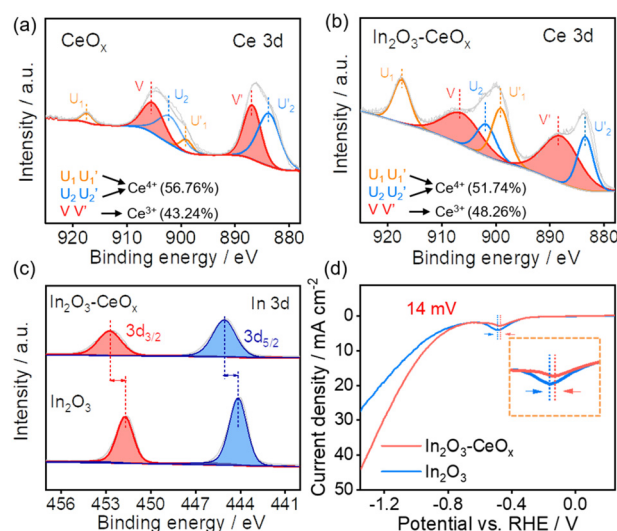


**Fig. 2** Ce 3d XPS spectra of (a)  $\text{CeO}_x$  and (b)  $\text{In}_2\text{O}_3\text{--CeO}_x$ ; (c) In 3d XPS spectra of  $\text{In}_2\text{O}_3\text{--CeO}_x$  and  $\text{In}_2\text{O}_3$ ; and (d) LSVs of  $\text{In}_2\text{O}_3$  and  $\text{In}_2\text{O}_3\text{--CeO}_x$  in  $\text{CO}_2$ -saturated 0.5 M  $\text{KHCO}_3$  at a scan rate of  $50\text{ mV s}^{-1}$ .

−0.487 V (vs. RHE), corresponding to a typical  $\text{In}^{3+}/\text{In}^0$  reduction peak (Fig. S4†).<sup>27</sup>

It should be noted that the reduction peak potential of  $\text{In}_2\text{O}_3\text{-CeO}_x$  positively shifted by 14 mV (appearing at −0.473 V) (Fig. 2d). The lower reduction potential of  $\text{In}_2\text{O}_3\text{-CeO}_x$  meant an enhanced electrochemical redox activity.<sup>28</sup> In contrast, no obvious change in the reduction peak potential was detected for  $\text{In}_2\text{O}_3\text{-CeO}_2$  compared to that of  $\text{In}_2\text{O}_3$  (Fig. S3c†). This result was consistent with the XPS data, revealing that the crystalline–amorphous heterostructure of  $\text{In}_2\text{O}_3\text{-CeO}_x$  led to stronger interactions between its individual components.

The electrocatalytic  $\text{CO}_2\text{RR}$  performances of  $\text{In}_2\text{O}_3$ ,  $\text{In}_2\text{O}_3\text{-CeO}_x$ , and  $\text{In}_2\text{O}_3\text{-CeO}_2$  were tested in a three-electrode system, with  $\text{CO}_2$  saturated 0.1 M  $\text{KHCO}_3$  as an electrolyte. Linear sweep voltammetry (LSV) curves were obtained at a scan rate of  $50 \text{ mV s}^{-1}$  between −1.38 V and −0.62 V (vs. RHE, all potentials used were vs. RHE unless otherwise stated). As depicted by the linear sweep voltammetry (LSV) curves of all catalysts (Fig. 3a and S5†), significantly higher current density was observed in  $\text{CO}_2$  than that under an Ar atmosphere, indicating that the  $\text{CO}_2$  reduction reaction occurred over these catalysts. Meanwhile, the current density of  $\text{In}_2\text{O}_3\text{-CeO}_x$  was larger than those of  $\text{In}_2\text{O}_3\text{-CeO}_2$  and  $\text{In}_2\text{O}_3$  in a  $\text{CO}_2$ -saturated electrolyte, indicating that a crystalline–amorphous  $\text{In}_2\text{O}_3\text{-CeO}_x$  heterostructure shows the best  $\text{CO}_2\text{RR}$  performance.

To further analyze the electroreduction products, controlled potential electrolysis of  $\text{CO}_2$  was performed at a constant working potential ranging from −0.6 V to −1.3 V. The gaseous and liquid products were quantified by gas chromatography (GC) and nuclear magnetic resonance (NMR) spectroscopy, respectively. For  $\text{In}_2\text{O}_3$ ,  $\text{In}_2\text{O}_3\text{-CeO}_2$  and  $\text{In}_2\text{O}_3\text{-CeO}_x$  catalysts, CO and  $\text{H}_2$  were detected as gas products, and formate was the

unique liquid product (Fig. S6†). The formate faradaic efficiency ( $\text{FE}_{\text{formate}}$ ) of the three catalysts all exhibited a volcano-like pattern over the range of applied operating potentials, among which, the  $\text{In}_2\text{O}_3\text{-CeO}_x$  electrode exhibited higher selectivity toward formate against  $\text{H}_2$  and CO (Fig. 3b and c). More remarkably, the  $\text{FE}_{\text{formate}}$  on the  $\text{In}_2\text{O}_3\text{-CeO}_x$  electrode remained above 90% over a wide electrochemical window from −0.8 V to −1.2 V. The maximum  $\text{FE}_{\text{formate}}$  reached 94.8% with a current density of  $7 \text{ mA cm}^{-2}$  at −0.9 V (Fig. 3c). By comparison, the maximum  $\text{FE}_{\text{formate}}$  for  $\text{In}_2\text{O}_3\text{-CeO}_2$  and  $\text{In}_2\text{O}_3$  electrodes was only 74.2% and 73.6%, respectively, under −1.0 V (Fig. S7a and b†). The optimal electrolysis potential of  $\text{In}_2\text{O}_3\text{-CeO}_x$  was more positive than that of  $\text{In}_2\text{O}_3$  and  $\text{In}_2\text{O}_3\text{-CeO}_2$ , which suggested that lower electrical energy was required to cross the energy barrier and realize the  $\text{CO}_2\text{RR}$  by the  $\text{In}_2\text{O}_3\text{-CeO}_x$  catalyst. Notably,  $\text{H}_2$  was the only product of the individual  $\text{CeO}_x$  and  $\text{CeO}_2$  (Fig. S7c and d†), indicating that the amorphous and crystalline ceria contributed to the formate formation *via* functions rather than being the catalyst.

The stability of  $\text{In}_2\text{O}_3\text{-CeO}_x$  was tested by continuous electrolysis at −0.9 V. As shown in Fig. 3d, no evident decay of current density and  $\text{FE}_{\text{formate}}$  was observed after 20 h-electrolysis, demonstrating the good stability of the prepared  $\text{In}_2\text{O}_3\text{-CeO}_x$  electrode. Moreover, the LSV curves before and after long-term test showed no obvious difference (Fig. S8†), which further manifested the good stability of  $\text{In}_2\text{O}_3\text{-CeO}_x$ . After the test, the element mapping of  $\text{In}_2\text{O}_3\text{-CeO}_x$  showed that In, Ce, and O were uniformly distributed (Fig. S9†). In addition, the HRTEM image of  $\text{In}_2\text{O}_3\text{-CeO}_x$  after electrolysis still showed the amorphous morphology of  $\text{CeO}_x$  and the (222) plane of  $\text{In}_2\text{O}_3$  (Fig. S9a and b†), indicating that the crystalline–amorphous heterostructure of  $\text{In}_2\text{O}_3\text{-CeO}_x$  can be retained during the electrolytic process.

To gain a deeper understanding of the kinetics of  $\text{CO}_2$  electroreduction, we fitted the overpotentials of the three catalysts as a function of the bias current density for formate production to obtain the corresponding Tafel slopes (Fig. 4a).  $\text{In}_2\text{O}_3\text{-CeO}_x$  presented a smaller calculated Tafel slope ( $176 \text{ mV dec}^{-1}$ ) compared to  $\text{In}_2\text{O}_3\text{-CeO}_2$  ( $186 \text{ mV dec}^{-1}$ ) and pure  $\text{In}_2\text{O}_3$  ( $375 \text{ mV dec}^{-1}$ ). The smallest Tafel slope of  $\text{In}_2\text{O}_3\text{-CeO}_x$  suggested the largest increment in the  $\text{CO}_2$  reduction rate with the increasing overpotential. The electron transfer properties were further investigated by an electrochemical impedance spectroscopy (EIS) test. As shown in Fig. 4b,  $\text{In}_2\text{O}_3\text{-CeO}_x$  showed smaller charge transfer resistance ( $R_{\text{ct}}$ ) compared to  $\text{In}_2\text{O}_3\text{-CeO}_2$  and  $\text{In}_2\text{O}_3$ . The results suggested that the crystalline–amorphous heterostructure rendered faster charge transfer than the bare  $\text{In}_2\text{O}_3$  and crystalline–crystalline heterostructure, and the interaction of electrochemically active  $\text{In}_2\text{O}_3$  with the amorphous  $\text{CeO}_x$  led to a more efficient electron transfer. The electrochemically active surface area (ECSA) was evaluated by the electrochemical double layer capacitance ( $C_{\text{dl}}$ ) due to their positive proportion relationship (Fig. 4c).<sup>2,29,30</sup> The ECSA of  $\text{In}_2\text{O}_3\text{-CeO}_x$  ( $13.75 \text{ cm}^2$ ) was higher than those of  $\text{In}_2\text{O}_3\text{-CeO}_2$  ( $11.50 \text{ cm}^2$ ) and  $\text{In}_2\text{O}_3$  ( $9.50 \text{ cm}^2$ ), which can promote the electrocatalytic performance. In addition, the

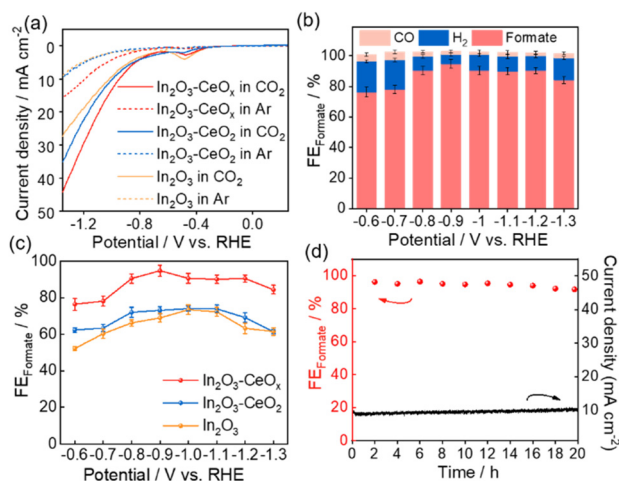


**Fig. 3**  $\text{CO}_2$  electroreduction in a 0.5 M  $\text{KHCO}_3$  electrolyte. (a) LSV curves of  $\text{In}_2\text{O}_3\text{-CeO}_x$ ,  $\text{In}_2\text{O}_3\text{-CeO}_2$  and  $\text{In}_2\text{O}_3$  electrodes in a  $\text{CO}_2$ -saturated electrolyte. (b) The  $\text{FE}_{\text{formate}}$ ,  $\text{FE}_{\text{CO}}$  and  $\text{FE}_{\text{H}_2}$  of  $\text{In}_2\text{O}_3\text{-CeO}_x$  at different applied potentials, respectively. (c)  $\text{FE}_{\text{formate}}$  of  $\text{In}_2\text{O}_3\text{-CeO}_x$ ,  $\text{In}_2\text{O}_3\text{-CeO}_2$  and  $\text{In}_2\text{O}_3$  at different applied potentials, respectively. (d) Long-term stability of the  $\text{CO}_2$  electroreduction for  $\text{In}_2\text{O}_3\text{-CeO}_x$  at −0.9 V (vs. RHE).



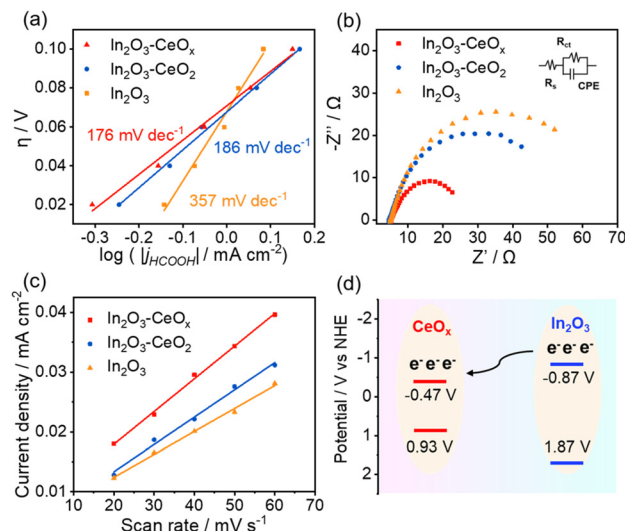


**Fig. 4** Advantages of  $\text{In}_2\text{O}_3\text{-CeO}_x$  for  $\text{CO}_2$  reduction. (a) Tafel plots, (b) Nyquist plots (inset: equivalent circuit), (c) linear fitting of double-layer capacitive currents versus scan rates to estimate the ECSA of  $\text{In}_2\text{O}_3\text{-CeO}_x$ ,  $\text{In}_2\text{O}_3\text{-CeO}_2$  and  $\text{In}_2\text{O}_3$ , and (d) schematic illustration of the charge transfer in  $\text{In}_2\text{O}_3\text{-CeO}_x$ .

partial current density of formate was normalized by the ECSA (Fig. S11†).<sup>2</sup> Similar to the geometric current density, the normalized current density of  $\text{In}_2\text{O}_3\text{-CeO}_x$  was the highest among the three samples. The rough surface of the  $\text{CeO}_x$  substrate promoted the adsorption and dispersion of  $\text{In}_2\text{O}_3$ , thereby increasing the active surface area. Furthermore, to verify the phenomenon of electron transfer between  $\text{In}_2\text{O}_3$  and  $\text{CeO}_x$  in  $\text{In}_2\text{O}_3\text{-CeO}_x$ , we performed Mott-Schottky and valence band XPS experiments (Fig. S12†). As shown in Fig. 4d, the flat band potentials of  $\text{In}_2\text{O}_3$  and  $\text{CeO}_x$  were located at  $-0.87$  V and  $-0.47$  V (vs. NHE), respectively. Such a band alignment can effectively facilitate the interfacial electrons transferring from the key component  $\text{In}_2\text{O}_3$  to  $\text{CeO}_x$ . However, the flat band and valence band potentials of  $\text{CeO}_2$  and  $\text{In}_2\text{O}_3$  were not significantly different (Fig. S13†), and thus electron transfer hardly occurred between  $\text{CeO}_2$  and  $\text{In}_2\text{O}_3$ .

Density functional theory (DFT) calculations were carried out to shed light on the origin of the enhanced activity of  $\text{In}_2\text{O}_3\text{-CeO}_x$  for the  $\text{CO}_2\text{RR}$  (Fig. S14–S16†). The charge density difference and charge displacement curves of  $\text{In}_2\text{O}_3\text{-CeO}_x$  and  $\text{In}_2\text{O}_3\text{-CeO}_2$  were obtained to study the transfer of electrons.<sup>31–33</sup> As shown in Fig. 5a, the positive and negative signals of the charge displacement curve represented electron accumulation and depletion, respectively. The  $\text{In}_2\text{O}_3\text{-CeO}_x$  heterostructure displayed a significant charge rearrangement around the crystalline–amorphous heterostructure interface, and electron transfer took place from  $\text{In}_2\text{O}_3$  to  $\text{CeO}_x$ , which was in good agreement with the XPS results. Moreover, the reaction pathways for the generation of formate were considered. According to the calculations, the Gibbs free energy for the rate-determining step (RDS) on  $\text{In}_2\text{O}_3\text{-CeO}_x$  is lower than that on  $\text{In}_2\text{O}_3\text{-CeO}_2$  and  $\text{In}_2\text{O}_3$  for the  $\text{CO}_2$ -to-formate

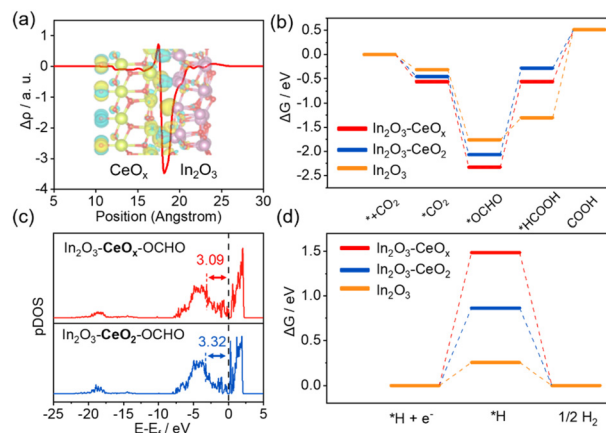


**Fig. 5** DFT calculations. (a) Charge density difference and charge displacement curves of  $\text{In}_2\text{O}_3\text{-CeO}_x$ ; purple, yellow, and red spheres represent In, Ce, and O atoms, respectively. (b) Gibbs free-energy diagrams of  $\text{CO}_2$ -to-formate. (c) In-5p p-DOS of  $\text{In}_2\text{O}_3\text{-CeO}_x$  and  $\text{In}_2\text{O}_3\text{-CeO}_2$  after adsorbing  $^*\text{OCHO}$ . (d) Gibbs free-energy diagrams of the HER.

process (Fig. 5b), suggesting that  $\text{In}_2\text{O}_3\text{-CeO}_x$  was thermodynamically more favourable for  $\text{CO}_2$ -to-formate conversion. The adsorption energies of the  $^*\text{OCHO}$  intermediates on  $\text{In}_2\text{O}_3\text{-CeO}_x$  and  $\text{In}_2\text{O}_3\text{-CeO}_2$  were further explained by the projected density of states (p-DOS). As shown in Fig. 5c, the centre of the p-band for  $\text{In}_2\text{O}_3\text{-CeO}_x\text{-}^*\text{OCHO}$  was closer to the Fermi level compared with that of  $\text{In}_2\text{O}_3\text{-CeO}_2\text{-}^*\text{OCHO}$ , which verified that the antibonding state filling of the In-5p orbital of  $\text{In}_2\text{O}_3\text{-CeO}_x$  is lower than that of  $\text{In}_2\text{O}_3\text{-CeO}_2$ , thereby enhancing the adsorption strength of  $^*\text{OCHO}$ .<sup>14</sup> In addition, the Gibbs free energy for the dominant competitive HER was also explored (Fig. 5d). The Gibbs free energy for generating  $^*\text{H}$  over  $\text{In}_2\text{O}_3\text{-CeO}_x$  was much larger than that for  $\text{In}_2\text{O}_3\text{-CeO}_2$  and  $\text{In}_2\text{O}_3$ , indicating that the HER was more difficult to occur on  $\text{In}_2\text{O}_3\text{-CeO}_x$ . Therefore, the crystalline–amorphous  $\text{In}_2\text{O}_3\text{-CeO}_x$  heterostructure accelerated the electron transfer, enhanced the adsorption to  $^*\text{OCHO}$ , lowered the energy barrier for the process from  $\text{OCHO}^*$  to  $^*\text{HCOOH}$ , and finally promoted the formation of the formate product. Furthermore, the  $\text{In}_2\text{O}_3\text{-CeO}_x$  catalyst significantly suppressed the HER competition reaction compared with  $\text{In}_2\text{O}_3$  and  $\text{In}_2\text{O}_3\text{-CeO}_2$ .

## Conclusion

In conclusion, we described a facile strategy to fabricate the crystalline–amorphous  $\text{In}_2\text{O}_3\text{-CeO}_x$  heterostructure and studied its performance for the  $\text{CO}_2\text{RR}$ . The experimental results showed that  $\text{In}_2\text{O}_3\text{-CeO}_x$  achieved better catalytic performance than the crystalline–crystalline  $\text{In}_2\text{O}_3\text{-CeO}_2$  heterostructure and  $\text{In}_2\text{O}_3$  alone. The maximum FE of 94.8% was achieved on the  $\text{In}_2\text{O}_3\text{-CeO}_x$  catalyst, and the FE remained above 90% over a wide potential range of  $-0.8$  to  $-1.2$  V vs. RHE. Detailed studies have shown that there was a remarkable electron transfer from  $\text{In}_2\text{O}_3$  to amorphous  $\text{CeO}_x$  on the  $\text{In}_2\text{O}_3\text{-}$

CeO<sub>x</sub> heterostructure compared to the crystalline-crystalline In<sub>2</sub>O<sub>3</sub>-CeO<sub>2</sub> heterostructure, which decreased the interfacial charge transfer resistance. The In<sub>2</sub>O<sub>3</sub>-CeO<sub>x</sub> heterostructure promoted the adsorption for \*OCHO intermediates and thereby the energy barrier of \*OCHO → \*HCOOH was reduced, which led to the high selectivity of the CO<sub>2</sub>RR to formate. We believe that the work may provide an effective strategy for catalysing CO<sub>2</sub> conversion.

## Conflicts of interest

There are no conflicts to declare.

## Acknowledgements

This work was supported by the National Natural Science Foundation of China (22007004, 22178019, 21625101 and 21521005), the National Key Research and Development Program of China (2017YFB0307303) and the Fundamental Research Funds for the Central Universities (buctrc202010, XK1802-6, XK1803-05, XK1902 and 12060093063).

## Notes and references

- 1 Y. Y. Birdja, E. Pérez-Gallent, M. C. Figueiredo, A. J. Göttle, F. Calle-Vallejo and M. T. M. Koper, Advances and challenges in understanding the electrocatalytic conversion of carbon dioxide to fuels, *Nat. Energy*, 2019, **4**, 732–745.
- 2 C. Chen, X. Sun, X. Yan, Y. Wu, H. Liu, Q. Zhu, B. B. A. Bediako and B. Han, Boosting CO<sub>2</sub> electroreduction on N,P-Co-doped carbon aerogels, *Angew. Chem., Int. Ed.*, 2020, **59**, 11123–11129.
- 3 W. Guo, X. Tan, J. Bi, L. Xu, D. Yang, C. Chen, Q. Zhu, J. Ma, A. Tayal, J. Ma, Y. Huang, X. Sun, S. Liu and B. Han, Atomic indium catalysts for switching CO<sub>2</sub> electroreduction products from formate to CO, *J. Am. Chem. Soc.*, 2021, **143**, 6877–6885.
- 4 Z. Wang, Y. Zhou, C. Xia, W. Guo, B. You and B. Y. Xia, Efficient electroconversion of carbon dioxide to formate by a reconstructed amino-functionalized indium-organic framework electrocatalyst, *Angew. Chem., Int. Ed.*, 2021, **60**, 19107–19112.
- 5 N. Han, P. Ding, L. He, Y. Li and Y. Li, Promises of main group metal-based nanostructured materials for electrochemical CO<sub>2</sub> reduction to formate, *Adv. Energy Mater.*, 2020, **10**, 1902338.
- 6 F. Valentini, V. Kozell, C. Petrucci, A. Marrocchi, Y. Gu, D. Gelman and L. Vaccaro, Formic acid, a biomass-derived source of energy and hydrogen for biomass upgrading, *Energy Environ. Sci.*, 2019, **12**, 2646–2664.
- 7 W. Guo, S. Liu, X. Tan, R. Wu, X. Yan, C. Chen, Q. Zhu, L. Zheng, J. Ma, J. Zhang, Y. Huang, X. Sun and B. Han, Highly efficient CO<sub>2</sub> electroreduction to methanol through atomically dispersed Sn coupled with defective CuO catalysts, *Angew. Chem., Int. Ed.*, 2021, **60**, 21979–21987.
- 8 L. Lu, W. Guo, C. Chen, Q. Zhu, J. Ma, H. Wu, D. Yang, G. Yang, X. Sun and B. Han, Synthesis of Sn<sub>4</sub>P<sub>3</sub>/reduced graphene oxide nanocomposites as highly efficient electrocatalysts for CO<sub>2</sub> reduction, *Green Chem.*, 2020, **22**, 6804–6808.
- 9 D. Yang, Q. Zhu, X. Sun, C. Chen, W. Guo, G. Yang and B. Han, Electrosynthesis of a defective indium selenide with 3D structure on a substrate for tunable CO<sub>2</sub> electroreduction to syngas, *Angew. Chem., Int. Ed.*, 2020, **59**, 2354–2359.
- 10 J. E. Pander, M. F. Baruch and A. B. Bocarsly, Probing the mechanism of aqueous CO<sub>2</sub> reduction on post-transition-metal electrodes using ATR-IR spectroelectrochemistry, *ACS Catal.*, 2016, **6**, 7824–7833.
- 11 J. Li, M. Zhu and Y.-F. Han, Recent advances in electrochemical CO<sub>2</sub> reduction on indium-based catalysts, *ChemCatChem*, 2021, **13**, 514–531.
- 12 Y. Huang, X. Mao, G. Yuan, D. Zhang, B. Pan, J. Deng, Y. Shi, N. Han, C. Li, L. Zhang, L. Wang, L. He, Y. Li and Y. Li, Size-dependent selectivity of electrochemical CO<sub>2</sub> reduction on converted In<sub>2</sub>O<sub>3</sub> nanocrystals, *Angew. Chem., Int. Ed.*, 2021, **60**, 15844–15848.
- 13 J. Zhang, R. Yin, Q. Shao, T. Zhu and X. Huang, Oxygen vacancies in amorphous InO<sub>x</sub> nanoribbons enhance CO<sub>2</sub> adsorption and activation for CO<sub>2</sub> electroreduction, *Angew. Chem., Int. Ed.*, 2019, **58**, 5609–5613.
- 14 Z. Chen, G. Yu, B. Li, X. Zhang, M. Jiao, N. Wang, X. Zhang and L. Liu, In situ carbon encapsulation confined nickel-doped indium oxide nanocrystals for boosting CO<sub>2</sub> electroreduction to the industrial level, *ACS Catal.*, 2021, **11**, 14596–14604.
- 15 W. Luo, W. Xie, R. Mutschler, E. Oveisi, G. L. De Gregorio, R. Buonsanti and A. Züttel, Selective and stable electroreduction of CO<sub>2</sub> to CO at the copper/indium interface, *ACS Catal.*, 2018, **8**, 6571–6581.
- 16 M. A. Ahsan, T. He, J. C. Noveron, K. Reuter, A. R. Puente-Santiago and R. Luque, Low-dimensional heterostructures for advanced electrocatalysis: an experimental and computational perspective, *Chem. Soc. Rev.*, 2022, **51**, 812–828.
- 17 P. Prabhu, V. Jose and J.-M. Lee, Heterostructured catalysts for electrocatalytic and photocatalytic carbon dioxide reduction, *Adv. Funct. Mater.*, 2020, **30**, 1910768.
- 18 A. Vasileff, C. Xu, Y. Jiao, Y. Zheng and S.-Z. Qiao, Surface and interface engineering in copper-based bimetallic materials for selective CO<sub>2</sub> electroreduction, *Chem*, 2018, **4**, 1809–1831.
- 19 P.-F. Sui, C. Xu, M.-N. Zhu, S. Liu, Q. Liu and J.-L. Luo, Interface-induced electrocatalytic enhancement of CO<sub>2</sub>-to-formate conversion on heterostructured bismuth-based catalysts, *Small*, 2022, **18**, 2105682.
- 20 Z. Zhang, F. Ahmad, W. Zhao, W. Yan, W. Zhang, H. Huang, C. Ma and J. Zeng, Enhanced electrocatalytic reduction of CO<sub>2</sub> via chemical coupling between indium

- oxide and reduced graphene oxide, *Nano Lett.*, 2019, **19**, 4029–4034.
- 21 J. Wang, X. Xiao, Y. Liu, K. Pan, H. Pang and S. Wei, The application of CeO<sub>2</sub>-based materials in electrocatalysis, *J. Mater. Chem. A*, 2019, **7**, 17675–17702.
  - 22 D. Gao, Y. Zhang, Z. Zhou, F. Cai, X. Zhao, W. Huang, Y. Li, J. Zhu, P. Liu, F. Yang, G. Wang and X. Bao, Enhancing CO<sub>2</sub> electroreduction with the metal–oxide interface, *J. Am. Chem. Soc.*, 2017, **139**, 5652–5655.
  - 23 H. Dong, L. Zhang, L. Li, W. Deng, C. Hu, Z.-J. Zhao and J. Gong, Abundant Ce<sup>3+</sup> ions in Au-CeO<sub>x</sub> nanosheets to enhance CO<sub>2</sub> electroreduction performance, *Small*, 2019, **15**, 1900289.
  - 24 S. Shen, Z. Wang, Z. Lin, K. Song, Q. Zhang, F. Meng, L. Gu and W. Zhong, Crystalline-amorphous interfaces coupling of CoSe<sub>2</sub>/CoP with optimized d-band center and boosted electrocatalytic hydrogen evolution, *Adv. Mater.*, 2022, **34**, 2110631.
  - 25 M. Yang, M. Zhao, J. Yuan, J. Luo, J. Zhang, Z. Lu, D. Chen, X. Fu, L. Wang and C. Liu, Oxygen vacancies and interface engineering on amorphous/crystalline CrO<sub>x</sub>-Ni<sub>3</sub>N heterostructures toward high-durability and kinetically accelerated water splitting, *Small*, 2022, **18**, 2106554.
  - 26 Y. X. Duan, Y. T. Zhou, Z. Yu, D. X. Liu, Z. Wen, J. M. Yan and Q. Jiang, Boosting Production of HCOOH from CO<sub>2</sub> Electroreduction via Bi/CeO<sub>x</sub>, *Angew. Chem., Int. Ed.*, 2021, **60**, 8798–8802.
  - 27 Z. M. Detweiler, J. L. White, S. L. Bernasek and A. B. Bocarsly, Anodized indium metal electrodes for enhanced carbon dioxide reduction in aqueous electrolyte, *Langmuir*, 2014, **30**, 7593–7600.
  - 28 F. Yang, X. Bao, P. Li, X. Wang, G. Cheng, S. Chen and W. Luo, Boosting hydrogen oxidation activity of Ni in alkaline media through oxygen-vacancy-Rich CeO<sub>2</sub>/Ni heterostructures, *Angew. Chem., Int. Ed.*, 2019, **58**, 14179–14183.
  - 29 Y. Wang, W. Zhou, R. Jia, Y. Yu and B. Zhang, Unveiling the activity origin of a copper-based electrocatalyst for selective nitrate reduction to ammonia, *Angew. Chem., Int. Ed.*, 2020, **59**, 5350–5354.
  - 30 C. Zhang, Y. Huang, Y. Yu, J. Zhang, S. Zhuo and B. Zhang, Sub-1.1 nm ultrathin porous CoP nanosheets with dominant reactive {200} facets: a high mass activity and efficient electrocatalyst for the hydrogen evolution reaction, *Chem. Sci.*, 2017, **8**, 2769–2775.
  - 31 G. Ciancaleoni, F. Nunzi and L. Belpassi, Charge displacement analysis-A tool to theoretically characterize the charge transfer contribution of halogen bonds, *Molecules*, 2020, **25**, 300–316.
  - 32 Y. Zhou, Y. Yao, R. Zhao, X. Wang, Z. Fu, D. Wang, H. Wang, L. Zhao, W. Ni, Z. Yang and Y. M. Yan, Stabilization of Cu<sup>+</sup> via strong electronic interaction for selective and stable CO<sub>2</sub> electroreduction, *Angew. Chem., Int. Ed.*, 2022, **61**, e202205832.
  - 33 D. Sorbelli, E. Rossi, R. W. A. Havenith, J. Klein, L. Belpassi and P. Belanzoni, Gold-alumanyl and gold-diarylboryl complexes: bonding and reactivity with carbon dioxide, *Inorg. Chem.*, 2022, **61**, 7327–7337.